

Particulates in NLC and PMSE during DROPPS 1 Flight: PID and PAT Sensors

J. Gumbel^a, H. D. Voss^{b*}, R. B. Sheldon^c, R. A. Goldberg^d, M. P. Assis^b, P. A. Webb^e, and W. D. Pesnell^d

^aMISU, Stockholm University, Svante Arrhenius vag 12, 10691 Stockholm, Sweden

^bTaylor University, 236 Reade Ave., Upland, IN 46989, USA

^cNASA/MSFC/NSSTC/USRA/VP62, 320 Sparkman Dr, Huntsville, AL 35805, USA

^dNASA/GSFC, Code 612.3, Greenbelt, MD 20771, USA

^eUniversity of Maryland, NASA/GSFC, Code 612.3, Greenbelt, MD 20771, USA

High-time resolution rocket measurements have been made of charged particulates under polar summer mesospheric conditions on 5 and 14 July 1999 during the DROPPS campaign at Andøya Rocket Range, Norway. Each rocket carried two Particle Trap (PAT) sensors, and two Particle Impact Detector (PID) telescopes with three biased grids, which were pointed into the rocket ram during both upleg and downleg. The Sun was within 51° of ram, providing a spin modulated UV input to both PID and PAT. The spin-averaged background current on PID grid 2 (-4 volt), and PAT is consistent with the altitude variation and flux expected for UV photoionization, with spin modulation able to separate the photoemission and particulate currents. DROPPS 1 was flown into a strong PMSE (polar mesospheric summer echo) condition with a weak NLC (noctilucent cloud) located at the base of the PMSE. Once the UV photoemission is removed from the data, both PAT and PID currents were consistent with each other and with the presence of uncharged, large ($10 < r < 50$ nm) ice grains in the NLC, and negatively charged, small ($1 < r < 10$ nm) ice grains in the PMSE. However the NLC analysis is complicated by a charging anomaly which we argue is a water-enhanced UV photoemission from the surface.

1. Introduction

Polar mesosphere summer echoes (PMSE) and noctilucent clouds (NLC) occur in the summer high latitudes mesosphere where temperatures can drop well below 130 K. NLCs, composed of large visible aerosol particles, usually appear in the altitude range 82 to 85 km, whereas PMSEs, composed of smaller subvisible particles, usually appear between 82 and 88 km. A review of PMSEs can be found in Cho and Kelley (1993); Cho and Röttger (1997); Rapp and Lübken (2004), and a review of NLCs can be found in Thomas (1991, 1995). PMSEs show strong radar returns between 50 MHz and >1 GHz and may

*hnvooss@taylor.edu Phone: 765 998 4843

be associated with layering of electrically charged ice aerosols. Some have suggested that the electron diffusion is reduced (Cho and Kelley, 1993; Rapp and Lübken, 2000) due to the charged aerosols, which would result in a variability of electron density and refractive index structure that can reflect radar. But the theory of PMSE generation Cho and Kelley (1993); Cho and Röttger (1997); Rapp and Lübken (2004), has not reached consensus on either the mechanism responsible for Bragg-reflected radar, the spatial structuring, or the location-specific occurrence statistics, in part because the composition remains ill-determined.

Early on, *in situ* measurements of what appear to be positive and negative charged aerosols made by Havnes et al. (1996b,a) using a double grid sensor, suggested a dust-enhanced internal electric field. Rapp and Lübken (1999) modeled aerosol charge collection on ice and metals, concluding that theoretically only pure sodium and potassium have low enough work functions to allow for significant photoionization and positively charged dust. Recent laboratory results for sub-micron particles (Abbas et al., 2003, 2006) revealed that a popular theory of positive aerosol production (Draine and Sutin, 1987), which relied on a theoretical extrapolation of experimental results from 10 microns down to 0.1 microns was unsupported. In fact, submicron particles were charged by UV in the same manner as the nanometer clusters described by atomic and molecular physics community, providing the theory of UV charging a smooth interpolation from atomic to macroscopic dimensions. Therefore there is little theoretical or laboratory support for positively charged aerosols in the mesosphere.

In his reanalysis of earlier data (Havnes, 2006) suggested that the observation of positive charge may be an instrumental artifact arising from a rocket-dust interaction. Therefore the existence of and mechanism for producing positive current in an NLC is an open question we address in this paper, though there is growing consensus that a PMSE is composed of negatively charged, subvisible ice grains.

Increased ionization and dynamics by energetic electrons may also play a role in PMSE (Kelley et al., 1990; Barabash et al., 2002), but no clear associations have been made statistically (Cho and Röttger, 1997; Morris et al., 2005). Progress in understanding PMSE generation will require high quality *in situ* data correlated with ground measurements. Therefore the DROPPS campaign, which coordinated extensive ground observations and *in situ* particulate density, charge, precipitating electron, composition and plasma parameters collected by the well-instrumented DROPPS rocket, has provided highly significant data. This paper addresses some of the complexities that have delayed the analysis of this comprehensive data set, as well as new evidence for dusty plasmas.

A schematic of the DROPPS (The **D**istribution and **R**ole of **P**articles in the **P**olar **S**ummer **M**esosphere) experiment is illustrated in Figure 1 and is described in detail by Goldberg et al. (2001). The DROPPS payload included an array of six booms as shown for DC and AC electric field measurements (Holzworth et al., 2001; Pfaff et al., 2001), Langmuir aft tip probes, blunt probes, radio propagation experiment, Gerdien sensors (Croskey et al., 2001; Mitchell et al., 2001), NLC photometers and a particle aerosol trap (PAT) detector (Waelchli et al., 1993; Gumbel and Witt, 1998). In addition, particulate and plasma charge and density sensors and an energetic electron sensor (PID) were included,. During the campaign, MIDAS, Mini-Dusty, and MET (Schmidlin and Schauer, 2001), were also launched with simultaneous ground-based data collected from

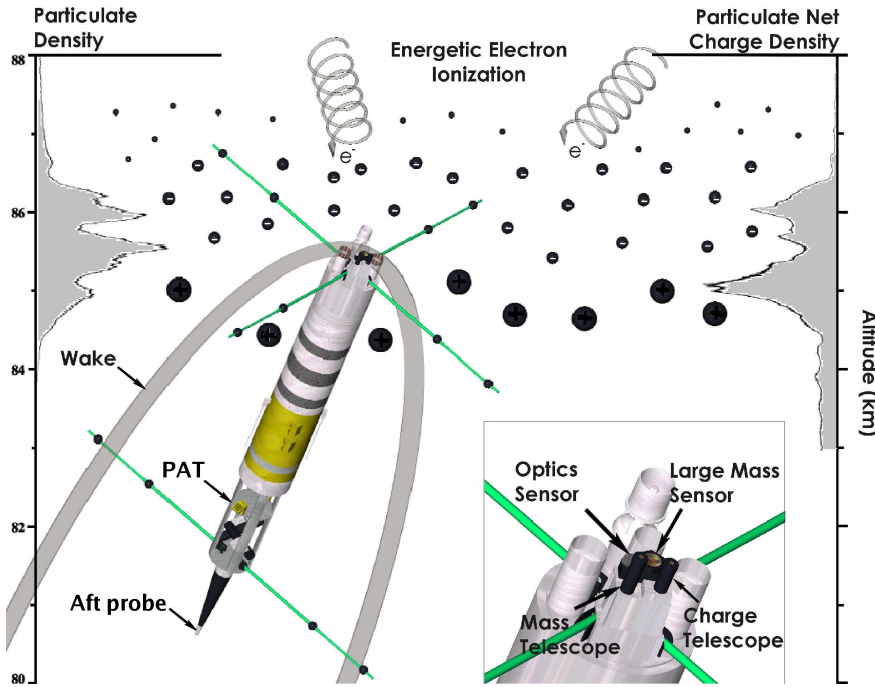


Figure 1. DROPPS rocket schematic, with inset on PID sensor.

the ALOMAR lidar, the ALOMAR MST radar (53.5 MHz), and the EISCAT radars (933 MHz and 224 MHz in Trømso, Norway) as discussed by Goldberg et al. (2001).

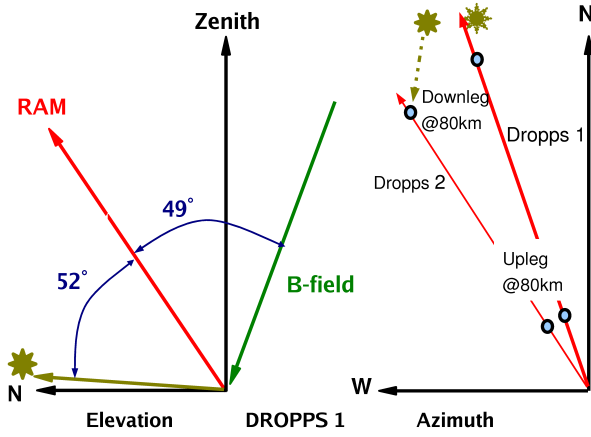


Figure 2. Rocket-sun geometry.

This paper focuses on the data recorded by the PAT (Particle Trap) and PID (Particle Impact Detector) on the first rocket (DROPPS 1) launched while a strong PMSE coupled with a weak NLC was in progress.

Table 1
PID and PAT instrument subsystems.

Name	Instrument	Characteristics
PAT1	Particle Trap 1	Graphite (aquadag) coated $\pm 3.9V$ 10 10x1cm slats
PAT2	Particle Trap 2	Gold coated $\pm 3.9V$ 10 10x1cm slats
CGRID1	Charge Telescope Grid 1	94.5% transp. SSteel Harp, +6V (Langmuir probe)
CGRID2	Charge Telescope Grid 2	94.5% transparent SSteel Harp, -4V 1.6 cm ²
CGRID3	Charge Telescope Grid 3	94.5% transparent SSteel Harp, +2.5V 1.6 cm ²
MGRID1	Mass Telescope Grid 1	as CGRID1 but +4V scanned Langmuir Probe
MGRID2	Mass Telescope Grid 2	as CGRID2
MGRID3	Mass Telescope Grid 3	as CGRID3
LPVDF	Large PVDF Detector	7 cm ²

2. Instrumentation

2.1. Particle Impact Detector (PID)

The DROPPS 1 Black Brant rocket was launched from Andøya, Norway (69.3° N 16.02° E, magnetic L shell of 6.2 at 100 km) on 5 July 1999 at 23:36:30 UT and achieved an apogee altitude of 117.3 km. After the nose cone and boom deployments, the attitude control system pointed the telescopes within a few degrees of the ram direction over the 80-90 km region of interest (Goldberg et al., 2001). The northward launch faced the sun in azimuth, and at 80km altitude had a 52° elevation above the sun direction. At apogee the attitude control tipped the rocket over to point in the downward ram direction, which made the sun angle about -39° in elevation (See Figure 2). This attitude control allowed continuous data with reduced spin modulation effects yielding unprecedented fine structure measurements.

The PID detectors were located at the top of the DROPPS payload (Figure 1 inset). The PID instrument package consisted of a charge telescope, a mass telescope, and a PVDF spectrometer. Table 1 gives additional instrument details. The polyvinylidene fluoride (PVDF) sensor is based on the principles of charge generation from depolarization and piezoelectric effect of a thin (6 micron thick) foil at the rocket impact velocities of about 1 km/s, which would be sensitive to particles greater than about 50 nm and densities greater than 100 cm^{-3} (Simpson and Tuzzolino, 1985; Tuzzolino, 1992).

The charge and mass telescopes consisted of three grids and a bottom sensor as shown in Figure 3. The instrument is similar to the pioneering work by Havnes et al. (1996b,a), but with much finer grid “harps” having 94.5% transmission and the addition of a third, positively biased grid. Each grid was connected to a sensitive logarithmic electrometer to monitor the net current.

2.1.1. Charge Telescope

The three grids in the Charge telescope are labeled CGRID1, CGRID2 and CGRID3. The first grid, CGRID1 held at +6 V, acts as a Langmuir probe for electrons but blocks the ions of mass-per-charge < 1000 amu/e (or positive singly charged ice grains $r < 0.6$ nm) from entering the telescope. The DROPPS 1 rocket was launched at an azimuth almost directly facing the sun, at 51° in elevation, allowing solar UV to illuminate the aluminum grid frames, so this grid also has a solar UV response. The frames are circular,

however, which tends to minimize the rocket spin modulation, but sensitive to nutation.

The second grid, CGRID2 at 4 V, is sandwiched between the two positive grids and responds to positively charged particulates, as well as impacting negative particulates that adhere to the thin grid wires (cross sectional area of 0.09 cm^2), UV photoemission, or impact generated negative ion emission. SIMION 3D simulations of charged particulates entering the PID at a rocket velocity of 1 km/s show that this second grid will repel negative particles with a mass/charge ratio less than 1100 amu/e, which corresponds to 1.1 nm diameter grains with the density of ice.

The third grid, CGRID3 at +2.5 V, responds to primary or secondary charges generated by particulates or particulate impacts below CGRID2. The currents measured with the CGRID1, CGRID2, and CGRID3 showed no cross talk during calibration, nor observed in flight, as seen by the strong spin-correlated UV signal on CGRID2 at apogee that was absent from CGRID1 and CGRID3.

2.1.2. Mass Telescope

The three grids in the Mass telescope are labeled MGRID1, MGRID2, and MGRID3. It is a big shorter than the Charge telescope, which may have a slight effect on the in-flight dynamics, but otherwise the two telescopes are dimensionally identical. The major difference is electrical, with the front grid swept in voltage from -5V to +4V in 75 ms and held at +4 V for 1083 ms. The sweeps allow both positive ions and smaller grains through the front grid, which add an exponentially decaying signal to MGRID2 but otherwise MGRID2 and MGRID3 are identic to CGRID2 and CGRID3.

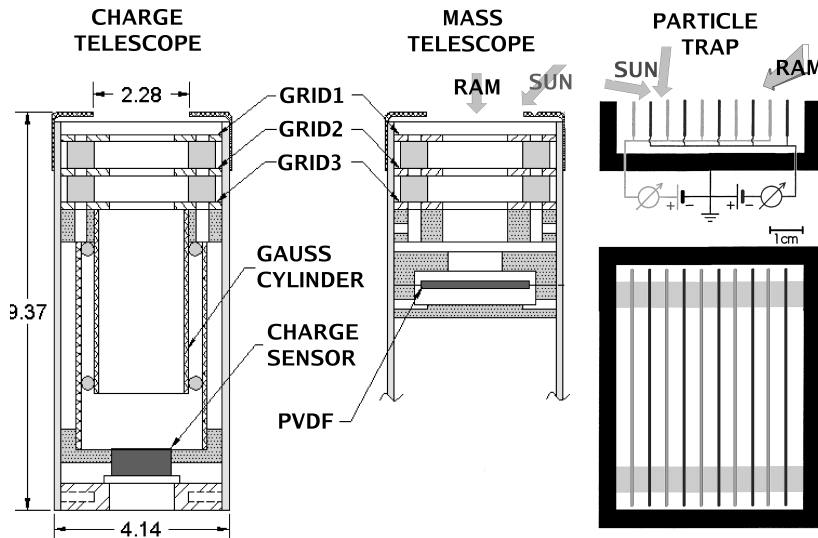


Figure 3. Schematic of PID and PAT with ram and sun directions. The PAT ram direction is in the plane of the paper.

2.2. Particle Trap Detector

Lower on the rocket body (Figure 1) were two Particle Trap (PAT) sensors of Stockholm University (Gumbel, 1997; Gumbel and Witt, 1998), which consisted of 10 slat electrodes aligned with the rocket axis mounted in an open box located at the side of the payload,

and hinged to deploy at $\sim 60^\circ$ from the rocket axis after launch. The slats were alternately biased at ± 3.9 V, and the current to payload ground was sensitively measured (Figure 3). Like the three grids of the Charge and Mass Telescopes, PAT collects current from charged particles or UV light without too much interference from the background electron density, being inside the rockets bow shock and plasma sheath. The PAT1 sensor is coated with graphite (aquadag) and the PAT2 sensor is gold-plated, surfaces that do not form oxide layers so that they have stable, though different, electron work functions.

3. Data

3.1. UV Photocurrents on CGRIDs and PAT

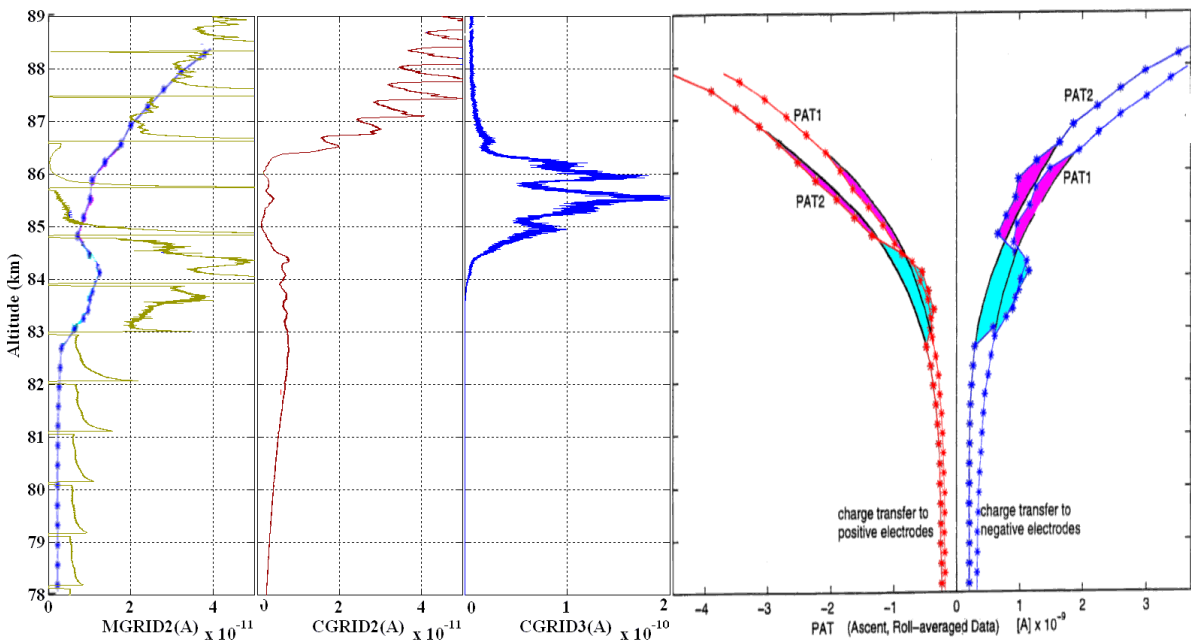


Figure 4. PID currents MGRID2, CGRID2, CGRID3, and PAT1/2 spin-averaged currents upleg. PAT negative electrode overlaid on MGRID2 with 0.01 current scaling.

In Figure 5, we plot the current on the positive and negative slats of the graphite-coated PAT1 clearly showing a spin modulation. Below 83 km, the spin-modulated total currents are nearly identical, with the positive slat showing a double-peaked current, whereas the negative slat has a stronger central peak with side lobes. This is simply a result of the sun-rocket geometry, Figures 2 & 3.

3.1.1. UV photoemission model

We argue that the production of photoelectrons, UV , is proportional to the intensity of the UV light landing on the slat surface, I , multiplied by an efficiency, η , and the illuminated surface area, A .

$$UV = \eta I A \quad (1)$$

If we designate the PAT slat's long axis \hat{m} , the slat's short axis \hat{o} , and the slat normal \hat{n} along the rocket axis \hat{z} , \hat{m} along \hat{y} , and \hat{o} along the rocket

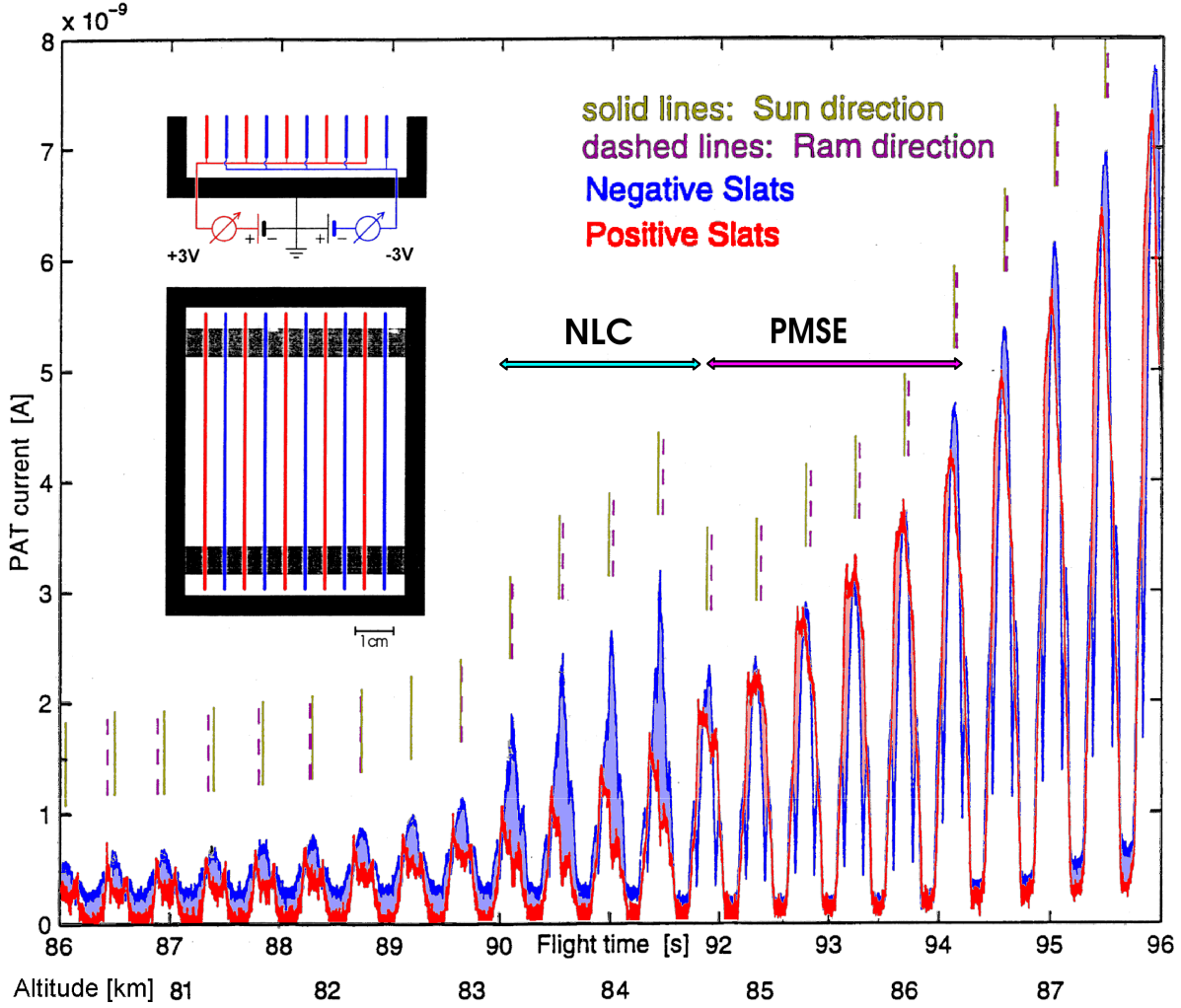


Figure 5. PAT1 measured current on positive(negative) slats in blue(red) as a function of time and altitude.

radius vector \hat{x} , where \hat{x} is defined to be in the plane containing the rocket and sun vectors. Then after launch the rotation of the rocket spin is around \hat{z} by an amount ωt , whereas the PAT sensor deploys by a pitch angle rotation $\theta = \sim 60^\circ$ about \hat{m} . (An alternative “Model 1, Vertical” was considered where the slats long dimension \hat{m} was aligned with the rocket axis, but it produced only double peaks, not triple peaks.)

The Euler angle matrix that defines the new PAT vectors is then:

$$(\hat{o}, \hat{m}, \hat{n}) = \begin{vmatrix} \cos(\omega t)\cos(\theta) & \sin(\omega t)\cos(\theta) & \sin(\theta) \\ -\sin(\omega t) & \cos(\omega t) & 0 \\ -\sin(\theta)\cos(\omega t) & -\sin(\theta)\sin(\omega t) & \cos(\theta) \end{vmatrix} \begin{vmatrix} \hat{x} \\ \hat{y} \\ \hat{z} \end{vmatrix} \quad (2)$$

The sun is taken to be $\phi = 51.6^\circ$ from the vertical, or a vector $\hat{s} = (\sin(\phi), 0, \cos(\phi))$, then we can compute the cosine of the sun vector with the slat long edge, \hat{m} , or with the slat normal, \hat{n} , or with the slat short edge \hat{o} , are:

$$\alpha = \hat{s} \cdot \hat{m} = -\sin(\phi) \sin(\omega t) \quad (3)$$

$$\beta = \hat{s} \cdot \hat{n} = -\sin(\phi) \cos(\omega t) \sin(\theta) + \cos(\phi) \cos(\theta) \quad (4)$$

$$\gamma = \hat{s} \cdot \hat{o} = \sin(\theta) \cos(\phi) + \cos(\theta) \sin(\phi) \cos(\omega t) \quad (5)$$

Then the intensity of UV light falling on the slat long edge and slat normal is,

$$I_m = I_0 \alpha^q \quad (6)$$

$$I_n = I_0 \beta^q \quad (7)$$

where I_0 is the normal incidence UV light intensity at this altitude, and q is some power-law correction for loss to specular reflection, where $q = 1$ for rough surfaces, but may approach $q = 2$ for smooth surfaces.

The illuminated area is the projected length and width of the 5 slats including shadowing effects, plus the one grounded side of the box that illuminated on the inside. The box side doesn't contribute to the plates that are providing the charge carriers, but does contribute to the plates that are collecting the charge carriers. We define the following illuminated areas providing $\gamma > 0$, otherwise 0. The illuminated depth of the slat is

$$D = 0.5\gamma/|\beta| \text{ cm} \quad (8)$$

or 1.0 cm, whichever is smaller. The illuminated length of the slat is

$$L = 10 - 1.0|\alpha|/\gamma \text{ cm} \quad (9)$$

or 0.0 cm, whichever is larger. And finally, the illuminated width (top edge) of the slat is

$$W = 0.09 \text{ cm} \quad (10)$$

So the illuminated area for emission of electrons is just the 5 plates that are charged negative including their edges, whereas the collection of electrons excludes the edges but must also include the illuminated ground box that can provide electrons in a region where the positive plates can collect them. Of course, the light falling on the box is shadowed by the slats, however if specular reflection is bouncing the UV off the slats, then the box is only partially shadowed. We model this partial shadow with the parameter, $\kappa = \cos(\beta) - \cos^q(\beta)$, so that the width of the illuminated floor area becomes:

$$F = 5.0 - 10 * 1.0 * |\beta|/\gamma - 10 * W \text{ cm}, \quad (11)$$

or 0.0 cm whichever is larger.

Then multiplying by the efficiency of photoelectron production and scaling the intensity with the cosine of the sun angle gives,

$$UV_- = I_0 \eta [5|\beta|^q(DL) + \gamma^q(WL)] \quad (12)$$

$$UV_+ = I_0 [\xi_s \eta 5|\beta|^q(DL) + \xi_f (10\kappa(DL) + \gamma^q 10F)] \quad (13)$$

where we fold in a collection efficiency for positive slats to grab electrons from negative slats, ξ_s , and another collection-emission efficiency for the electrons generated by the ground box, ξ_f . Using the model parameters listed in the Table 2, we plot the photoemission current (in arbitrary units) in Figure 6.

Table 2
PAT UV photoemission parameters

η	0.8	efficiency for photoemission
ξ_f	0.5	collection*production efficiency from box
ξ_s	0.8	electron collection efficiency from slats
θ	60°	PAT pitchangle after deployment
ϕ	51.6°	Sun Angle
ω	18.85 /s	rocket angular spinrate
q	1.0	specular reflection powerlaw
width	5.5 cm	width of the PAT box
length	10 cm	length of PAT box
depth	1 cm	depth of PAT box
thick	0.09 cm	thickness of slats

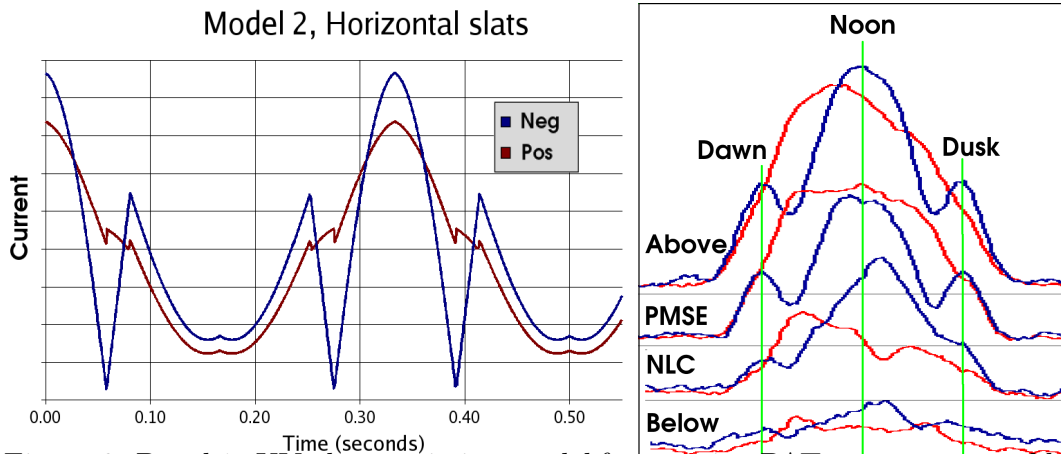


Figure 6. Panel 1: UV photoemission model for rotating PAT sensor mounted horizontally. Red are positive slats, blue negative slats as a function of time. Panel 2: Close up of four peaks in the PAT modulated currents: above, PMSE, NLC, and below. Thin blue curves are currents on the negative slats, wide red curves are currents on the positive slats. Increasing intensity with altitude is both due to increased UV intensity and electron mobility.

3.1.2. Model Comparison with Data

When $t \rightarrow 0.15s$, the PAT sensor goes into rocket shadow, and $UV \rightarrow 0$, an effect we have not included in the model. The model assumes that photoelectrons are the sole source of current, and most of them are collected. Then the asymmetry of current between positive and negative slats seen below 83km in Figure 5, is attributed to the differing efficiency for current production and collection, the negative slat being the cathode, and the positive slat the anode. Diffusive losses to the rocket sheath mean that the cathode may produce more current than the anode collects. (In this analysis, we have ignored the backscattered light from the cloud discussed below, which would tend to “fill-in” the minima seen in the “side illumination” curves.)

In addition to explaining the current collection asymmetry, this analysis also clearly suggests that the primary current carriers are negative, since the negative slats have

larger net currents than the positive slats. It also suggests that the current carriers are behaving diffusively, for in the absence of collisions, nearly all the current should appear on the positive slat. Collisions, however, diffuse charge that normally would be collected into the rocket sheath, reducing the current collected by the anode. Thus the collection efficiency, ξ , should increase with altitude, and explains how the positive electrode more closely approaches the negative electrode at highest altitudes.

3.2. PAT surface modification in the NLC

In the NLC, however, the photocurrent on the negative slats shows a large increase, but the current on the positive slats does not. Note also how the double peaked current on the positive slats becomes asymmetric, suggesting that whatever is increasing the photoemission for negative slats is asymmetrically affecting positive slats. Above the NLC, the excess photocurrent on the negative slats diminish, whereas the positive slats seem to get more efficient for normal incidence, eventually mimicking the photoemission curves of the negative slats, which we take to be the signature of reduced collisions.

The current seen on the dark side of the rocket, in the spin-modulation minima, are either from diffusing photocurrent, scattered UV, or charged particles. Tracing the dark-side minima then, one sees a broad peak on the negative slat that diminishes above the NLC, but is absent in the positive slat. Since this broad peak does not have the sharp boundaries of either the NLC or the PMSE, but does have the same shape as the photometer profiles, we attribute it to UV that is scattered by the NLC/PMSE. Note that if this offset is subtracted uniformly from the negative slat, the photocurrents on the two slats appear to line up quite well below 83 km.

Thus there appear to be three competing processes in the PAT currents: 1) a negative excess dark current below 84 km; 2) a negative excess photocurrent in the middle of the NLC at 83-84 km; and 3) an asymmetric collection efficiency of the positive slat that improves with altitude. We tentatively assign the causes of these three effects to a) scattered UV light below 84 km, b) ice/water modification of the surface work function (asymmetric on the positive slats); and c) a reduction in pressure with altitude that increases the electron mobility and hence collection efficiency. Note that if ice particulates in the NLC are responsible for increasing the UV photocurrent efficiency in (b), they are simultaneously vaporizing, reducing the mobility and collection efficiency in (c).

If we integrate over the spin modulation, we can see the effects of particulates and height dependence with greater clarity.

3.2.1. Dry spin-averaged PAT net currents

In Figure 4, we plot the spin-averaged currents on the positive (red) and negative (blue) slats, overplotting the graphite PAT1 with the gold PAT2. Note that there is a persistent offset between the two sensors, which we attribute to the different work functions for the two sensors. That is, the currents are dominated by the photocurrents that exponentially increase with height, so the more electronegative work function of graphite, which is less willing to free a photoelectron, will create smaller currents on the negative graphite slats, and larger currents on the positive graphite slats, so both PAT1 curves shift toward the right. We interpret this offset as a DC voltage bias proportional to the difference between the graphite and gold work functions.

Since the gold slats draw more negative current than the graphite slats, it would seem

to suggest that the PAT2 is gaining charge at the expense of PAT1. However, charge neutrality (or current continuity) is supplied by currents through the rocket plasma sheath, such that the net charge on the rocket (and the PAT sensors) remains constant. So with respect to the aluminum skin of the rocket, which is the ground of the PAT instrument and the zero of the current scale, the graphite is an electron generator and the gold an electron sink. Then the pair of PAT sensors function as a solar cell on the rocket skin producing ~ 0.4 V of potential.

Given the predictable nature of UV flux as a function of altitude, and the fixed voltage difference between the pair of PAT sensors, we can plot the expected spin-averaged photocurrent as a black line in these plots (Figure 4). Deviations from this smooth profile are found in the altitude range where NLC/PMSE particles impact on the electrodes. Enhanced electron emission (light blue) dominates at 83.0-84.5 km, while suppressed negative current (light red) dominates at 84.5-86.5 km. In Figure 4, we overplot the negative PAT2 slat with the negative MGRID2 grid showing that these profiles are in remarkable agreement, i.e. a positive bay in the NLC and a negative bay in the PMSE, though MGRID2 shows a greater sensitivity to aerosols.

To understand this effect, we constructed a simple model of the PAT photocurrents where we assume that the rocket photocurrent, I , is nearly independent of rocket potential, because the production of photoelectrons is unaffected by a few volts on the aluminum skin. To achieve equilibrium, the rocket potential, V_R , rises to draw in enough cold plasma electrons to neutralize the escaping hot photoelectrons. Since the aluminum surface area of the rocket far exceeds that of the PAT sensors, V_R is nearly independent of PAT configuration. The net current of an entire PAT sensor is the sum of negative and positive plates, and if the sensor were made of aluminum, we would expect the net current to be zero, as the rocket is itself. Net currents different from zero would then be due to net potentials/ work functions different from V_R , and would be proportional to the surface area, since UV photocurrents are proportional to area. That is:

$$i_j = (V_R - V_j)\eta_j A_j \quad (14)$$

Then fast changes to the net current in the PAT sensors would be either due to changes in the voltage difference, or changes in the photoemission efficiency, η . Outside the NLC, the gold plated PAT2 had a net current slightly more negative than the aluminum rocket, whereas PAT1 had a net current more positive than the rocket. The work function for aquadag (Taft and Apker, 1955), suggests values 4.65-4.85 eV, but when mixed with bentonite, (an aluminum silicate) it increases to 5.2-5.5 eV. However, Taft and Apker (1955) point out that the spectra of photoemitted electrons is quite different than most metals, such that it acts as if its work function is practically higher. The work function for polished aluminum is 3.9-4.08eV, but even 3nm of oxide raise that value to 4.3eV. Anodizing aluminum is a process whereby thick oxide layers, up to 200nm can be added to aluminum, and is generally used for exposed aluminum surfaces, which we presume to be the case for the DROPPS rocket. Even the noble metal gold has a work function depending on deposition method, (Sachtler et al., 1966), with 5.3 eV being a typical polycrystalline value. Given these uncertainties, we estimate 4.9eV for aquadag, 5.3eV for gold, and we estimate the aluminum workfunction by assuming that the photoefficiency and area are the same for PAT1 and PAT2, such that $i_2/i_1 = (V_2 - V_R)/(V_1 - V_R)$. Solving

for the rocket potential, we have

$$V_R = (i_1 V_2 - i_2 V_1) / (i_1 - i_2) \quad (15)$$

The effective rocket potential we have calculated is measured from the plasma frame, and includes the work function. In Table 3 we plots the inferred rocket potential and measured “skin” potential (Holzworth et al., 2001) as a function of altitude. To eliminate the disturbances in the NLC and PMSE, we used a smooth curve to fit the unperturbed PAT currents in Figure 4 and in the Table indicated these interpolations with an asterisk. In the last column, we add together the measured skin potential and the inferred work function, deriving a number consistent with a constant, which should characterize the unchanging aluminum work function of the rocket skin. This suggests that the PAT analysis below and above the NLC/PMSE is not contaminated by changing efficiencies or effective areas.

Table 3
PAT net currents, estimated and measured rocket potential

Altitude km	i_{Au} nA	i_C nA	Est. W_R eV	Meas. V_R V	* i_{Au} nA	* i_C nA	*Est. W_R eV	Sum V
78	-.04	0.14	5.21					
79	-.04	0.16	5.22					
80	-.07	0.17	5.18	-.13				5.05
81	-.09	0.16	5.16	-.12				5.04
82	-.13	0.18	5.13	-.10				5.03
82.5	-.15	0.20	5.13	-.09				5.04
83	+.13	0.27	5.70	-.08	*-.22	*0.18	*5.08	*5.00
83.5	+.48	0.51	11.56	-.04	*-.27	*0.17	*5.06	*5.02
84	+.58	0.43	3.73	0.00	*-.33	*0.35	*5.10	*5.10
84.5	-.12	0.06	5.04	0.10	*-.42	*0.12	*4.99	*5.09
85	-.78	-.21	4.75	0.00	*-.50	*0.08	*4.95	*4.95

* Interpolated from data as if dry.

3.2.2. Wet spin-averaged PAT currents

Now the offset between PAT1 and PAT2 due to differing UV work functions is constant at all altitudes and in the negative bay of the PMSE, except in the positive bay of the NLC, where the offset vanishes. If the excess current in the NLC were due to positive charged aerosols, the amount should be identical in PAT1 and PAT2, which would still be offset by the differing photocurrents. Instead, we see both PAT sensors producing the same amount of current in the NLC. Therefore we take the vanishing offset in the positive bay of the NLC to be an indication that the surfaces of PAT1 and PAT2 have temporarily been given the same UV work function, which by inspection, must be smaller than graphite, or $W < 4.8$ eV, a value we associate with the water/ice deposited by the NLC.

From Gumbel et al. (2001) we estimate that the NLC ice particle density of $3000/\text{cm}^3$ of 20 nm grains over a half kilometer of cloud, roughly the time it takes to see PAT respond,

amounts to $\sim 5\%$ coverage by a monolayer of molecules at normal incidence. Since one would expect the work function to be a weighted average of the areas, and since ice has a higher work function than most materials, theoretically icing should decrease the current. So the increased currents and decreased work function must be due to something other than an ice-modified surface work function.

If instead of ice, we have water on the surface, the work function would be very different. It is difficult to determine the work functions of volatile liquids because the photocurrents are usually measured in a vacuum. For if the water is evaporating, and if every water molecule carries off one electron, then this would create an evaporation current, which for the conditions listed above, would be $I > 10\text{mA}$, or about 10^4 times greater than the PAT spin-averaged current of 1nA . Of course, evaporating water is usually neutral, or we could get electricity from boiling eggs on the stove, but clearly it provides another channel for UV photoemission not available to a passive gold or graphite surface. Therefore the reduced work function in the NLC might be understood as the ability for evaporating water to enhance the photoemission rate.

Before we construct a theory, we consider an alternative mechanism suggested by Havnes (2006) that the ice grains carry off the charge by a triboelectric process after an elastic collision, in contrast to our suggestion of an inelastic collision followed by transport of charge in the vapor. The two mechanisms might be seen as endpoints on a continuum, with breakup and fragmentation of the ice grains or water cluster ions having characteristics of both elastic and inelastic collisions. So without bias, both mechanisms are simplifications of a collisional process that can be tested by experiment.

Vostrikov et al. (1987) carried out lab experiments with water cluster ions (nanometer-sized charged water particles) impacting at 1 km/s onto various surfaces. They found that ion production efficiency per molecule was about 10^{-7} for small 300 molecule clusters, increasing to an asymptotic 10^{-4} for 1500 molecule clusters, which consistent with our 10^4 overestimate above. However, they also found that positive water ion production usually exceeded negative water ion production, at least on gold and aluminum surfaces. Since this result is opposite to the rocket data, further experiments were conducted.

Andersson and Pettersson (1997) extended the work to graphite, and showed that heating the surface to $\sim 1300\text{ K}$ greatly enhanced the negative ion production. These results were explained with a thermal model of the electrons: When the surface is cold, hot electrons evaporated by impact ionization preferentially condense on the cold surface producing net positive ions; but when the surface is hot, evaporating electrons from the hot surface preferentially condense on the escaping water producing net negative ions. They model the ionization fraction with the Arrhenius equation:

$$\frac{f_-}{f_0} = A_- \exp[-(\phi - EA)/k_B T] \quad \frac{f_+}{f_0} = A_+ \exp[-(IP - \phi)/k_B T] \quad (16)$$

where f_- , f_+ , f_0 is the flux of negative, positive ions and neutrals, A_- , A_+ is the ratio between the partition functions of the ionic and neutral state of the species, EA is the electron affinity, IP is the ionization potential of the desorbing water cluster, ϕ is the surface work function, k_B is Boltzmann's constant, and T the surface temperature. For the laboratory experiment, $\phi_{GRAPHITE} = 4.55\text{ eV}$, and $EA = 1.4 \pm 0.3\text{ eV}$ rising asymptotically with size to 1.65 eV . For this experiment, $IP = 5.1 \pm 0.1\text{ eV}$. and that at an

elevated temperature of ~ 1320 K, the positive and negative currents were equal.

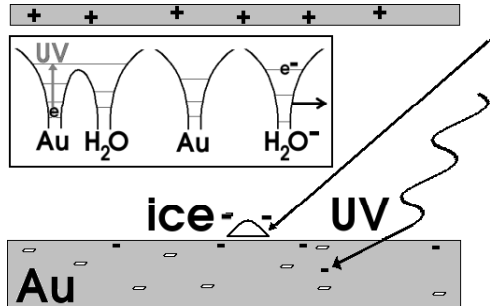


Figure 7. Schematic water enhanced UV photoemission.

Even at Mach 3, neither the rocket skin nor the PAT sensor came close to 1320 K, but they were exposed to UV light. Although Vostrikov et al. (1987); Andersson and Pettersson (1997) did not carry out the experiment with UV light, the physics of photoemission is straightforward to include. UV photons absorbed by the metal slats liberate hot electrons that diffuse to the surface with slightly degraded energy. These electrons form a sparse, supra-thermal, non-equilibrium population within the metal that act just the same as the 1320 K thermal electrons in the laboratory experiment, only hotter. That is, they can easily tunnel through the surface work-function potential onto evaporating water molecules as schematically depicted in Figure 7. We assign them an effective temperature that is slightly higher for gold than graphite (due to details of the Fermi levels of the two conductors), but is essentially Lyman- α energy of 1 eV, or 11700 K, which is an order of magnitude higher than the negative current cross-over temperature. Because of this large temperature, one can approximate the exponential with the first term in the power law expansion, rederiving the photoemission equation with a modified work function reduced by the electron affinity, e.g. the work function for a wet surface, albeit scaled with the flux of water cluster ions impacting.

Thus the model predicts that when an ice or water cluster ion strikes the PAT plates in darkness, a weak negative current is generated, but in the presence of UV, a stronger positive current is produced. The voltage put on the slats does not prevent this charge from forming, but will affect the collection of the charges that were formed in this manner. Accordingly, triboelectric charging might be distinguished from UV emission in this data set by the asymmetry on the biased slats. Because the kinetic energy of an NLC ice grain is ~ 100 keV, elastic collisions will be symmetric on both positive and negative slats, removing as much charge from the negative slats as they deposit on the positive slats with or without UV, whereas water-enhanced UV photoemission will possess distinct spin modulation on the negative slats, while the positive slats only collect the negative charge made elsewhere.

3.2.3. Wet spin-modulated PAT currents

Examination of the charge collection on positive slats as a function of spin phase (Figure 5) shows clear asymmetries in the NLC. From Figure 6, we see that at 89 km, the positive slat currents are generally double peaked, since at spin-phase “noon”, more negative current is lost to the rocket sheath, suppressing the currents collected by the positive slat. However at 90 km in the NLC, the two positive slat peaks become asymmetric, where

the left-hand “dawn” peak remains at its nominal value, but the right-hand “dusk” peak becomes noticeably suppressed. By 91 km above the NLC the photoemission is carried by unhindered electrons with high mobility, and both dawn and dusk peaks are equally strong. This can also be seen in Figure 5 if a line is drawn to connect successive dawn peaks or dusk peaks.

We interpret this suppression of the “dusk” positive slat peak as a consequence of water vapor, evaporated by sunlight, changing the mobility of the negative ions or electrons coming from the negative slats. Since the time required for water vapor at these densities and temperatures to diffuse 0.5cm to fill the space between the slats is <5ms, the asymmetry is not due to a diffusion timelag, but rather the thermal inertia timelag of the slats as they rotate into sunlight. Since this asymmetry of the double-peaked positive slat current only occurs in the NLC, it suggests that wetting of the slats only occurs in the NLC, consistent with the previous calculation of UV-enhanced photoemission.

Therefore both the asymmetries in phase, and asymmetries between positive and negative plates support the theory that it is a surface modification in the NLC responsible for the charging anomaly.

3.3. Charged ice grains in the PMSE

CGRID2 at negative voltage measures both net charge density, and photocurrent. The front CGRID1 is biased to +6 V, or greatly above the rocket potential, and the primary barrier repelling ions. Above the PMSE region, CGRID2 currents are purely photocurrents, increasing with altitude as the UV intensity increases. Within the PMSE region, the reduced current observed could be: d) a reduction in large positive particles that make it through the first grid; e) an increase in heavy negative particles that impact on the 7% opaque grids; or, f) a suppression of the photocurrent. Since we dont see any evidence within the PMSE for large positive grains, we eliminate the first option. Should there be a population of heavy negative ions, they should track CGRID3 very closely, at an amplitude of 10%. Examination of Figure 4 shows that there is a rough correlation between CGRID2 and CGRID3, but not a detailed correlation. Therefore we tentatively assign the reduced current to (f), a reduced photocurrent.

Closer examination of the upleg correlation with CGRID3, show that three peaks in CGRID3 correspond to two peaks and a valley in CGRID2. If CGRID3 is responding to a single factor, then there appear to be two factors on CGRID2, one correlated and one anti-correlated. On the assumption that the broad decrease in CGRID2 is the same effect (f) seen on the PAT positive plates, on CGRID1 and on the aft-probe, namely water vapor suppression of collected current, then the partial recovery toward higher current is in phase with CGRID3, though at only 1-2% of the amplitude. This could be a consequence of: g) higher positive plasma density; h) positively charged dust; or i) the same enhanced photocurrents as seen on PAT. The positive potential of CGRID1 would seem to eliminate (g), and theoretical support for (h) is weak, which leaves (i) pending more detailed SIMION calculations of ice particle transport to CGRID2.

On the downleg, below the PMSE in the NLC region, (Figure 4) we see a net increase in the CGRID2 current that was not apparent in the upleg, perhaps because outgassing on the upleg was still occurring in the PID telescope. This increase in the NLC current is very similar to PAT, which showed increased current on the negative-biased slats for both up-

and downlegs. Since PAT is on the exterior of the rocket, outgassing on the upleg would be minimal, making it consistent with the CGRID2 data. However, as we discussed above, most of the PAT increase was an enhancement of the photoemission peak, suggesting that much of the CGRID2 enhancement may also be an enhanced photoemission effect, which at least on PAT, was greater than the dark current from potential ions.

Having eliminated positive dust as an explanation for the response in both CGRID2 and PAT, the other clear signature is in CGRID3, showing a current from negatively charged dust density of about $10,000/\text{cm}^3$. This is the same signature seen in the PAT sensor, explaining the negative bay of the PMSE as a result of negatively charged particles collected by the 50 cm^2 area of PAT at normal incidence. Using the density from CGRID3 gives a peak 1 nA on PAT, which after spin-averaging is about 0.2 nA, a value entirely consistent with the current decrease in the negative bay of the PMSE region. Note that the negative slats show a greater decrease in current than the positive slats show an increase. If the PMSE ice grains had coated the surface, as in the NLC, we would have expected the opposite effect. Yet if the ice grains had vaporized, and electrons were collected by PAT, the positive slat would also show the greater effect. We interpret this strange behavior of a larger bay on the negative slat to be evidence that the current carriers are negative ions, probably water ions. A calculation of the minimum velocity of a negative water ion necessary to overcome a 3.4 volt potential barrier gives about 590 m/s, or less than the rocket speed but greater than the shock-heated thermal speed. This suggests that even heavier negative ions are needed, perhaps water-cluster ions. The presence of such heavy ions would, of course, also suppress the photocurrents collected by the positive slat, thereby explaining the asymmetry of positive and negative slats.

4. Summary and Conclusions

The DROPPS 1 experiment has greatly improved our understanding of PMSE and NLC. In this paper we have reported on new instrumentation that has measured relationships between NLC and PMSE particulate density variations, in particular, the good agreement between PAT and PID sensors. Both sensors respond to UV light, which we show is not an impediment to analysis, but can be understood in terms of the work function of the sensors. Once this well understood background is removed from the PAT and PID sensors, both show a clear signal of negatively charged dust in the PMSE of about $10,000/\text{cm}^3$ if the grains are taken to be singly charged.

However, there appears to be a strong interaction between the larger ice particles of the NLC and UV light that dominates in the NLC, but has no effect in the PMSE, an effect that has been misinterpreted in the past as positively charged grains. Theory doesn't support positively charged dust grains, and now the consensus is that some other mechanism is responsible for this anomaly. Two theories for this charging anomaly have been discussed, a triboelectric charging by ice grains (Havnes, 2006), and a water-enhanced UV photoemission (Voss et al., 2006). In this paper we have presented evidence that this effect might be better explained by a surface effect of water than a triboelectric effect.

5. Acknowledgements

We thank Mr. Dave Prentice for his engineering work in building much of the instrument and working out the many interface requirements. We also thank Ken Kiers, Stan Burden, Jeff Dailey, Ragan Bach, and a number of students for their help in analysis, design and fabrication of the instruments. We thank the Wallops flight team under the leadership of Bruce Scott for their excellent integration and accommodation of a new instrument. We thank Andy Platt, John Lee, David Voss, and Jonathan Voss for helping with data analysis. We acknowledge the Taylor Research Training Program for supporting much of the data analysis. This work was supported at Taylor University under NASA grant NAG5-5184 and at the University of Washington under NAG5-5183.

References

- Abbas, M. M., Craven, P. D., Spann, J. F., Witherow, W. K., West, E. A., Gallagher, D. L., Adrian, M. L., Fishman, G. J., Tankosic, D., LeClair, A., Sheldon, R., Thomas, E., Jun. 2003. Radiation pressure measurements on micron-size individual dust grains. *J. Geophys. Res.* 108, 2–1.
- Abbas, M. M., Tankosic, D., Craven, P. D., Spann, J. F., LeClair, A., West, E. A., Weingartner, J. C., Tielens, A. G. G. M., Nuth, J. A., Camata, R. P., Gerakines, P. A., Jul. 2006. Photoelectric Emission Measurements on the Analogs of Individual Cosmic Dust Grains. *Astrophys. J.* 645, 324–336.
- Andersson, P. U., Pettersson, J. B. C., 1997. Ionization of water clusters by collisions with graphite surfaces. *Z. Phys. D* 41, 57–62.
- Barabash, V., Kirkwood, S., Chilson, P. B., Apr. 2002. Are variations in PMSE intensity affected by energetic particle precipitation? *Ann. Geophys.* 20, 539–545.
- Cho, J. Y. N., Kelley, M. C., Aug. 1993. Polar mesosphere summer radar echoes - Observations and current theories. *Reviews of Geophysics* 31, 243–265.
- Cho, J. Y. N., Röttger, J., 1997. An updated review of polar mesosphere summer echoes: Observation, theory, and their relationship to noctilucent clouds and subvisible aerosols. *J. Geophys. Res.* 102, 2001–2020.
- Croskey, C. L., Mitchell, J. D., Friedrich, M., Torkar, K. M., Hoppe, U.-P., Goldberg, R. A., Apr. 2001. Electrical structure of PMSE and NLC regions during the DROPPS program. *Geophys. Res. Lett.* 28, 1427–1430.
- Draine, B. T., Sutin, B., Sep. 1987. Collisional charging of interstellar grains. *Astrophys. J.* 320, 803–817.
- Goldberg, R. A., Pfaff, R. F., Holzworth, R. H., Schmidlin, F. J., Voss, H. D., Tuzzolino, A. J., Croskey, C. L., Mitchell, J. D., Friedrich, M., Murtagh, D., Witt, G., Gumbel, J., von Zahn, U., Singer, W., Hoppe, U.-P., Apr. 2001. DROPPS: A study of the polar summer mesosphere with rocket, radar and lidar. *Geophys. Res. Lett.* 28, 1407–1410.

- Gumbel, J., 1997. Rocket-borne optical measurements of minor constituents in the middle atmosphere. Ph.D. Thesis.
- Gumbel, J., Stegman, J., Murtagh, D. P., Witt, G., Apr. 2001. Scattering phase functions and particle sizes in noctilucent clouds. *Geophys. Res. Lett.* 28, 1415–1418.
- Gumbel, J., Witt, G., 1998. In situ measurements of the vertical structure of a noctilucent cloud. *Geophys. Res. Lett.* 25, 493–496.
- Havnes, O., 2006. On the observation of mesospheric dust particles by rocket probes. In: 36th COSPAR Scientific Assembly. pp. 3568–+.
- Havnes, O., Næsheim, L. I., Hartquist, T. W., Morfill, G. E., Melandsø, F., Schleicher, B., Trøim, J., Blix, T., Thrane, E., Oct. 1996a. Meter-scale variations of the charge carried by mesospheric dust. *Planet. Space Sci.* 44, 1191–1194.
- Havnes, O., Trøim, J., Blix, T., Mortensen, W., Næsheim, L. I., Thrane, E., Tønnesen, T., May 1996b. First detection of charged dust particles in the Earth's mesosphere. *J. Geophys. Res.* 101, 10839–10848.
- Holzworth, R. H., Pfaff, R. F., Goldberg, R. A., Bounds, S. R., Schmidlin, F. J., Voss, H. D., Tuzzolino, A. J., Croskey, C. L., Mitchell, J. D., von Cossart, G., Singer, W., Hoppe, U.-P., Murtagh, D., Witt, G., Gumbel, J., Friedrich, M., Apr. 2001. Large electric potential perturbations in PMSE during DROPPS. *Geophys. Res. Lett.* 28, 1435–1438.
- Kelley, M. C., Hall, T., Ulwick, J. C., Roettger, J., Inhester, B., Nov. 1990. Intense turbulence in the polar mesosphere - Rocket and radar measurements. *J. Atm. Terrestrial Phys.* 52, 875–891.
- Mitchell, J. D., Croskey, C. L., Goldberg, R. A., Apr. 2001. Evidence for charged aerosols and associated meter-scale structure in identified PMSE/NLC regions. *Geophys. Res. Lett.* 28, 1423–1426.
- Morris, R. J., Terkildsen, M. B., Holdsworth, D. A., Hyde, M. R., Dec. 2005. Is there a causal relationship between cosmic noise absorption and PMSE? *Geophys. Res. Lett.* 32, 24809–+.
- Pfaff, R., Holzworth, R., Goldberg, R., Freudenreich, H., Voss, H., Croskey, C., Mitchell, J., Gumbel, J., Bounds, S., Singer, W., Latteck, R., Apr. 2001. Rocket probe observations of electric field irregularities in the polar summer mesosphere. *Geophys. Res. Lett.* 28, 1431–1434.
- Rapp, M., Lübken, F.-J., Jul. 1999. Modelling of positively charged aerosols in the polar summer mesopause region. *Earth, Planets, and Space* 51, 799–807.
- Rapp, M., Lübken, F.-J., Oct. 2000. Electron temperature control of PMSE. *Geophys. Res. Lett.* 27, 3285–3288.

- Rapp, M., Lübken, F.-J., Dec. 2004. Polar mesosphere summer echoes (PMSE): Review of observations and current understanding. *Atmospheric Chemistry & Physics* 4, 2601–2633.
- Sachtler, W. M. H., Dorgelo, G. J. H., Holscher, A. A., Oct. 1966. The work function of gold. *Surface Science* 5 (2), 221–229.
- Schmidlin, F. J., Schauer, A. G., Apr. 2001. Mesospheric clouds and the neutral atmosphere during the 1999 DROPPS/MIDAS Campaign. *Geophys. Res. Lett.* 28, 1411–1414.
- Simpson, J. A., Tuzzolino, A. J., 1985. Polarized polymer films as electronic pulse detectors of cosmic dust particles. *Nucl. Inst. Meth.* A236, 187–202.
- Taft, E., Apker, L., September 1955. Photoelectric emission from polycrystalline graphite. *Phys. Rev.* 99 (6), 1831–1832.
- Thomas, G. E., Nov. 1991. Mesospheric clouds and the physics of the mesopause region. *Reviews of Geophysics* 29, 553–575.
- Thomas, G. E., 1995. Climatology of Polar Mesospheric Clouds: Interannual Variability and Implications for Long-Term Trends. The upper Mesosphere and Lower Thermosphere: A Review of Experiment and Theory, *Geophysical Monograph* 87, pp. 185–+.
- Tuzzolino, A. J., Jun. 1992. PVDF copolymer dust detectors: particle response and penetration characteristics. *Nuclear Instruments and Methods in Physics Research A* 316, 223–237.
- Voss, H. D., Webb, P. A., Pesnell, W. D., Goldberg, R. A., Gumbel, J., Assis, M. P., Sheldon, R. B., 2006. Particulate and plasma variations in nlc and pmse during dropps 1 and 2 flights. In: 36th COSPAR Scientific Assembly. pp. 3336–+.
- Vostrikov, A. A., Dubov, D. Y., Predtechenskii, M. R., 1987. Ionization of water clusters by surface collisions. *Chem. Phys. Lett.* 139, 124–128.
- Waelchli, U., Stegman, J., Witt, G., Cho, J. Y. N., Miller, C. A., Kelley, M. C., Swartz, W. E., Dec. 1993. First height comparison of noctilucent clouds and simultaneous PMSE. *Geophys. Res. Lett.* 20, 2845–2848.